

# Comparison of two- and three-dimensional reconstruction methods in optical tomography

Martin Schweiger and Simon R. Arridge

We present a three-dimensional (3D) image reconstruction scheme for optical near-infrared imaging of highly scattering material. The algorithm reconstructs the spatial distribution of the optical parameters of a volume  $\Omega$  from transillumination measurements on the boundary of  $\Omega$ . We test the performance of the method for a cylindrical object with embedded absorbing perturbation for a number of different source and detector arrangements. Furthermore, we investigate the effect of a mismatched reconstruction, using a two-dimensional (2D) reconstruction model to image a single plane of the object from 3D tomographic data obtained in a single plane. The motivation for the application of 2D models is their advantage in speed and memory requirements. We found that the difference in the measurement data between 2D and 3D models depends greatly on the measurement type used, giving a much better agreement for mean time-of-flight data than for dc intensity data. Image artifacts that are due to data model mismatches can therefore be significantly reduced by use of mean time data. © 1998 Optical Society of America

*OCIS codes:* 110.3080, 170.3010, 170.3880, 170.6920.

## 1. Introduction

Near-infrared imaging provides a means to reconstruct the spatial distribution of the absorption and scattering coefficients of biological tissue. Because these are directly related to the oxygenation state of blood and tissue, this technique can be used as a functional imaging modality. Applications include localized continuous monitoring of cerebral oxygenation of infants during and after birth,<sup>1,2</sup> brain activation studies during mental or physical exercises,<sup>3</sup> oxygenation consumption in muscle,<sup>4</sup> and breast imaging.<sup>5,6</sup>

Various reconstruction methods, including back-projection<sup>7-9</sup> and semianalytic<sup>10,11</sup> and linear schemes,<sup>12</sup> have been proposed. However, light transport in biological tissues in the optical and near-infrared wavelength range is scatter dominated, leading to essentially diffuse photon propagation. This makes the application of direct image recon-

struction techniques difficult, so increasingly attention is turning to iterative, optimization-based reconstruction methods.<sup>13-15</sup>

Iterative schemes consist of a forward model of light propagation, which maps a given solution of absorption and scatter coefficients to the corresponding boundary measurements, and an optimization routine that seeks to minimize the data error by iteratively modifying the solution. Generally, the diffusion approximation to the radiative transfer equation is employed as the forward model, whereas a choice of standard optimization methods, including Newton-type and conjugate gradient methods, can be used to solve the inverse problem.

Iterative techniques have so far been generally limited to two-dimensional (2D) problems because of the computational effort involved in the reconstruction. These 2D image reconstruction implementations are frequently evaluated with data simulated by a 2D light transport model to avoid a mismatch between the data and the inverse model.<sup>16,17</sup> One could hope to extend this approach to a tomographic scheme to reconstruct three-dimensional (3D) objects of an arbitrary shape by employing a tomographic setup that collects boundary data in a single plane at a time and then uses a 2D reconstruction program to produce the cross-sectional image in this plane, thereby forming a full 3D reconstruction as a series of 2D cross sections.

Recent research has shown that 2D reconstruction methods can recover optical parameters quantita-

---

M. Schweiger is with the Department of Medical Physics and Bioengineering, University College of London, 11-20 Capper Street, London WC1E 6JA, UK. S. R. Arridge is with the Department of Computer Science, University College of London, Gower Street, London WC1E 6BJ, UK.

Received 12 March 1998; revised manuscript received 18 June 1998.

0003-6935/98/317419-10\$15.00/0

© 1998 Optical Society of America

tively in geometries where the object shape and optical parameters vary in only two spatial dimensions, e.g., absorbing and scattering rods embedded in a cylindrical object and aligned with the cylinder axis.<sup>14,18,19</sup> However, these results either use difference data from two experiments with and without the rods present or use a calibration measurement on a homogeneous object to parameterize the model; in both approaches therefore, the availability of a reference set is presumed. We show in this paper that 2D difference reconstructions from 3D data yield better reconstruction results than absolute reconstructions and that the latter can fail even to localize embedded perturbations qualitatively (Subsections 3.C and 3.D). In restricted geometries, where calibration data are available, or where only localization rather than absolute quantitation is required, 2D methods can provide acceptable results.

In the case of a full 3D reconstruction problem with arbitrary parameter distributions, however, it is not obvious that a tomographic approach based on separate reconstructions of 2D slices is adequate because light will be scattered out of the imaging plane, and measurements will therefore be affected by the distribution of optical coefficients above and below the imaging plane. This is a fundamental difference to imaging modalities such as x-ray-computed tomography, where scatter is negligible or can be eliminated and where 2D reconstructions from single-plane data are therefore appropriate.

To date, 3D reconstructions have been limited to semianalytic methods that do not work well for nonlinear problems.<sup>20</sup> In this paper we present a 3D finite-element forward model and present 3D reconstructions acquired with this model. A number of different issues are of current interest, such as measurement type, algorithm type, noise model, and regularization. In this paper we explore just one issue: two versus three dimensions, keeping the other system parameters constant. Specifically, we demonstrate the effect of different measurement geometries on the reconstruction performance, and we test the limitations of mismatched reconstructions, i.e., 2D reconstruction of 3D data, for different measurement types.

## 2. Implementation

### A. Forward Model

We describe light transport in scattering tissue by the diffusion approximation to the transport equation,

$$\frac{\partial \Phi(\mathbf{r}, t)}{\partial t} - \nabla \cdot c(\mathbf{r})\kappa(\mathbf{r})\nabla \Phi(\mathbf{r}, t) + c(\mathbf{r})\mu_a(\mathbf{r})\Phi(\mathbf{r}, t) = q_0(\mathbf{r}, t), \quad \forall \mathbf{r} \in \Omega, \quad (1)$$

which defines the time-dependent photon density  $\Phi(\mathbf{r}, t)$  in terms of the absorption coefficient  $\mu_a(\mathbf{r})$ , diffusion coefficient  $\kappa(\mathbf{r}) = \{3[\mu_a(\mathbf{r}) + \mu_s'(\mathbf{r})]\}^{-1}$ , reduced scattering coefficient  $\mu_s'(\mathbf{r})$ , and speed of light  $c(\mathbf{r}) = c_0/\nu(\mathbf{r})$ , where  $\nu(\mathbf{r})$  is the refractive index and  $c_0$

the speed of light in a vacuum. The model uses Robin boundary conditions of the form

$$\Phi(\xi) + 2\kappa A \nabla_n \Phi(\xi) = 0, \quad \forall \xi \in \partial\Omega, \quad (2)$$

where  $n$  is the direction of the outward normal to the boundary  $\partial\Omega$  of  $\Omega$  at  $\xi$ . Boundary reflections are accommodated by the term  $A$  that depends on the refractive indices of the tissue and surrounding medium.<sup>21</sup>

We assume a time-of-flight data-acquisition setup, where the source term  $q_0$  represents an ultrashort pulse of light at time  $t_0$  at a point  $\zeta$  on  $\partial\Omega$ ,

$$q_0(\mathbf{r}, t) = \delta(\mathbf{r} - \zeta)\delta(t - t_0), \quad \zeta \in \partial\Omega. \quad (3)$$

When the source represents a collimated beam of light rather than a diffuse point source, it is common to represent this in the diffusion model as an isotropic point source at a depth  $z_0$  of 1 mean scattering length below the point of incidence,  $\zeta$ :  $z_0 = \mu_s'(\zeta)^{-1}$ . The boundary measurement of time-dependent exitance  $\Gamma(\xi, t)$  at a point  $\xi \in \partial\Omega$  is related to  $\Phi$  by Fick's law,

$$\Gamma(\xi, t) = -c(\xi)\kappa(\xi)\nabla_n \Phi(\xi, t). \quad (4)$$

The time-dependent measurement signal  $\Gamma(\xi, t)$  is usually referred to as temporal point-spread function. Although discrete samples of  $\Gamma$  in  $t$  could be used in principle to represent the data vector for the reconstruction, this is inefficient as the lack of high-frequency components in  $\Gamma$  suggests a high degree of redundancy in the temporally sampled data. Instead we propose the use of different integral transforms of  $\Gamma(t)$ , such as the time-integrated intensity  $E(\xi) = \int_0^\infty \Gamma(\xi, t)dt$  and the mean time of flight  $\langle t \rangle(\xi) = E^{-1}(\xi) \int_0^\infty t\Gamma(\xi, t)dt$ , as well as other measurement types.<sup>22,23</sup> Computationally efficient ways to calculate these transforms can be found that eliminate the need to calculate  $\Gamma(t)$  explicitly.<sup>24,25</sup> This is essential for the application of these data types in a reconstruction scheme that requires the repeated solution of the forward problem.

The simultaneous reconstruction of both  $\mu_a$  and  $\kappa$  is a major problem even in two dimensions because of the difficulty of separating the parameters,<sup>26</sup> and it requires use of at least two different measurement types.<sup>23</sup> Because this is a separate line of research, we restrict this initial study to the reconstruction of a single parameter,  $\mu_a$ , that can be achieved with a single data type. In this paper we use intensity ( $E$ ) and mean time ( $\langle t \rangle$ ) data. These are complementary to use of phase shift and modulation depth in the frequency domain.<sup>27</sup> The choice of data type turns out to have a significant influence on the 3D reconstruction performance (Subsection 3.B) and is particularly important in the case of a mismatched reconstruction of 3D data with a 2D reconstruction model (Subsection 3.C).

### B. Mesh Generation

In this paper we consider a cylindrical object:

$$\Omega = [(x, y, z)|x^2 + y^2 \leq a^2 \wedge -h/2 \leq z \leq h/2]. \quad (5)$$

This geometry allows a direct comparison between 2D and 3D problems. More-irregular shapes will be required to model actual body parts, but construction of these is entirely one of mesh generation, adding little to the forward and inverse problems themselves.

Figure 1 shows the mesh geometry used for the examples in this paper. The cylinder has radius  $a = 25$  mm and height  $h = 100$  mm. It consists of 17,724 nodes and 30,888 prism-shaped elements, divided into 11 layers. The cross section is equivalent to a 2D circular mesh with elements arranged in 16 concentric rings.

We previously presented the finite-element representation of the diffusion equation [Eq. (1)] for the 2D case.<sup>28,29</sup> The 3D case does not add any principal problems other than extending methods previously defined for triangular elements to prism elements. We define a standard prism element in a local coordinate system  $(x', y', z')$  so that its vertex coordinates are given by

$$\begin{aligned} N_1 &= (1, 0, -1), & N_2 &= \left(-\frac{1}{2}, -\frac{\sqrt{3}}{2}, -1\right), \\ N_3 &= \left(-\frac{1}{2}, \frac{\sqrt{3}}{2}, -1\right), \\ N_4 &= (1, 0, 1), & N_5 &= \left(-\frac{1}{2}, -\frac{\sqrt{3}}{2}, 1\right), \\ N_6 &= \left(\frac{1}{2}, \frac{\sqrt{3}}{2}, 1\right), \end{aligned} \quad (6)$$

and the shape functions  $u_i(x', y', z')$  associated with node  $i$  and support over the volume of the element are

$$\begin{aligned} u_1(x', y', z') &= \frac{1}{6} (1 + 2x')(1 - z'), \\ u_2(x', y', z') &= \frac{1}{6} (1 - x' - \sqrt{3}y')(1 - z'), \\ u_3(x', y', z') &= \frac{1}{6} (1 - x' + \sqrt{3}y')(1 - z'), \\ u_4(x', y', z') &= \frac{1}{6} (1 + 2x')(1 + z'), \\ u_5(x', y', z') &= \frac{1}{6} (1 - x' - \sqrt{3}y')(1 + z'), \\ u_6(x', y', z') &= \frac{1}{6} (1 - x' + \sqrt{3}y')(1 + z'). \end{aligned} \quad (7)$$

The integration of products of shape functions over the volume of the element, and surface integrals over a side of the element, as required for the computation of element stiffness and mass matrices, is performed by a numerical integration rule.<sup>30</sup> The mapping of shape functions and their integrals from local to global coordinates is a standard procedure in the finite-element method (FEM) (see, for example, Ref.

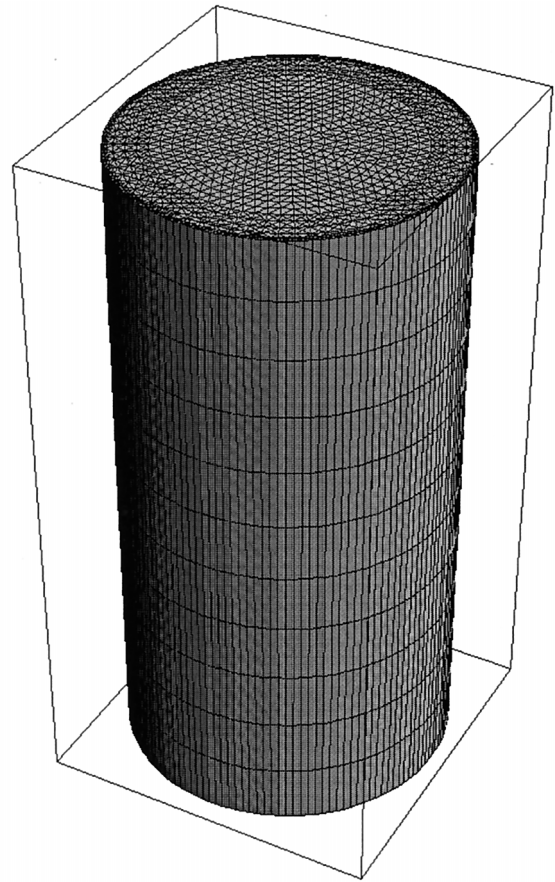


Fig. 1. Mesh structure of the cylindrical test object.

31). Once the element matrices are computed, the FEM model proceeds as in the 2D case without the need for any further alteration.

The main reason why 3D models have not been considered so far is the high computational cost caused by the large number of elements required. As we have shown previously, an accurate and stable FEM implementation of the diffusion model requires a high mesh resolution for typical optical parameters. For 2D models the computation time and storage requirements are within the limit of a workstation computer, but for 3D models they can be prohibitive. Memory requirements are predominantly defined by the  $D \times D$  system matrices, where  $D$  is the number of nodes in the mesh. The matrices are sparse, with the number of nonzero entries per line given by the number of neighbors for the corresponding node. For the mesh geometry used here, the number of entries per line is typically 30, leading to a total number of approximately 53,000 entries per matrix. We use a sparse matrix representation to exploit this and a conjugate gradient method to solve the FEM equation.<sup>32</sup>

### C. Inverse Model

We employ an iterative image reconstruction scheme that repeatedly calculates an update of the solution until an objective function, given by the sum of

squared differences between the measured data and the data calculated for the current solution, is acceptably small. The problem thus becomes one of minimization of the objective function. Various standard methods can be employed to solve this. Previously we presented Newton-like algorithms such as Levenberg–Marquardt that involve repeated construction and inversion of the problem Jacobian. The explicit calculation and inversion of the Jacobian becomes intractable when the number of parameters of the optimisation problem is large. This difficulty can be overcome by the use of algebraic reconstruction technique methods that operate in a row-by-row fashion. These methods can be implemented efficiently by employing an adjoint scheme to calculate the rows of the Jacobian, as presented previously.<sup>33,34</sup> In problems where the storage overhead of these methods is still too costly, gradient methods can be employed that require only the computation of the gradient of the objective function.<sup>35</sup> For the 3D reconstructions presented in this paper we therefore adopted a nonlinear conjugate gradient (CG) method, using a Polak–Ribiere scheme to generate search directions and an inexact quadratic interpolation scheme for the line minimization.<sup>36</sup>

### 3. Results

#### A. Measurement Geometry

For the following tests we consider the cylinder to consist of a homogeneous background medium with  $\mu_a = 0.025 \text{ mm}^{-1}$ ,  $\kappa = 0.165 \text{ mm}^{-1}$  equivalent to a reduced scattering coefficient of  $\mu_s' = 2 \text{ mm}^{-1}$  and a refractive index  $\nu = 1.4$ . Embedded into the background medium are three small perturbations with increased absorption,  $\mu_a = 0.1 \text{ mm}^{-1}$ . The perturbations are of cylindrical shape, with a radius of 1.4 mm and a height of 9.1 mm, corresponding to the height of a single-element layer. The objects are placed in the cylinder so that their centers are at positions  $(-6.25, -10.83, -18.2)$ ,  $(0, 12.5, 0)$ ,  $(6.25, -10.83, 18.2)$ , respectively (see Fig. 2).

Sources and detectors are placed in ring arrangements around the circumference of the cylinder. Each ring contains 16 sources and 16 detectors, equidistantly spaced, where each detector is located between two sources. We tested configurations with between one and five source–detector rings at different heights to test the influence of the measurement

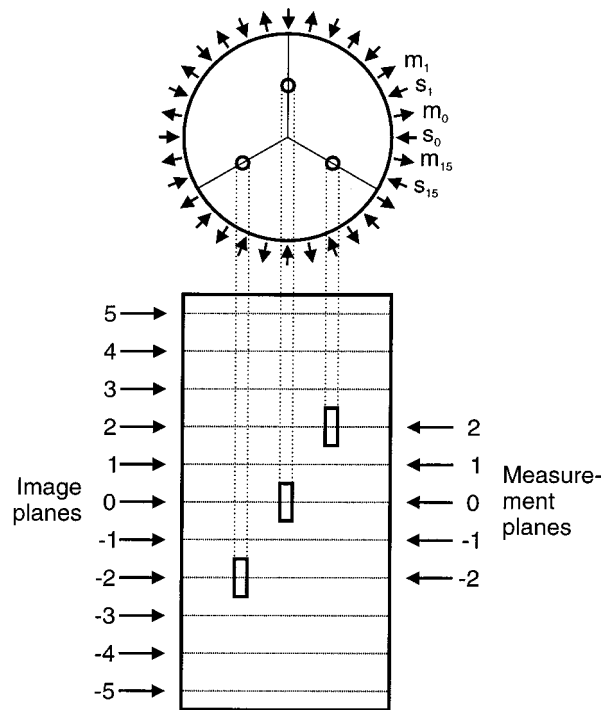


Fig. 2. Placement of  $\mu_a$  perturbations in the cylinder. Image planes indicate the locations of the 11 cross sections representing the 3D image in Figs. 3–7 and Fig. 9. Measurement planes indicate the locations of the planes at which measurement sites are located on the circumference of the cylinder. For the measurement configurations used, see Table 1.

geometry on the reconstruction performance. This ring arrangement is an obvious choice for a cylindrical geometry, but by no means the only one, nor necessarily the best. We show these results to demonstrate the potential of the 3D reconstruction scheme, but more research is necessary to find optimal measurement patterns in 3D problems.

#### B. Three-Dimensional Reconstruction from Different Measurement Geometries

We present reconstructions from data obtained from measurements in different acquisition planes, as described in Subsection 3.A. The number and locations of the measurement plane arrangements tested are listed in Table 1.

A series of 11 cross-sectional 3D reconstructions are presented, each corresponding to an element

Table 1. Measurement Geometries for 3D Cylinder Reconstructions<sup>a</sup>

Configuration ( $Q \times M \times P$ )	Measurement Planes	$z$ Positions (mm)	Number of Measurements
$16 \times 16 \times 1$	0	0	256
$16 \times 16 \times 2$	-2, 2	$\pm 18.2$	512
$16 \times 16 \times 3$	-2, 0, 2	$0, \pm 18.2$	768
$16 \times 16 \times 5$	-2, -1, 0, 1, 2	$0, \pm 9.1, \pm 18.2$	1280

<sup>a</sup>The total number of measurements is given by the product of the number of sources ( $Q$ ), detectors ( $M$ ), and measurement planes ( $P$ ). The measurement planes refer to the plane indices introduced in Fig. 2. The  $z$  positions denote the elevations of the measurement planes above and below the central plane of the cylinder ( $z = 0$ ).

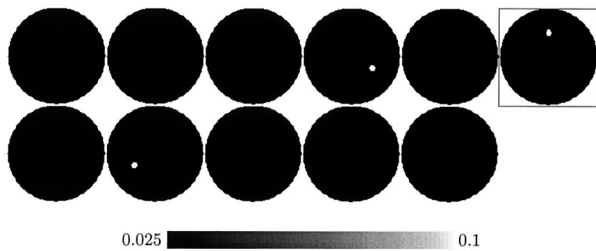


Fig. 3. Target  $\mu_a$  image for 3D reconstructions: 11 horizontal slices through a cylindrical object containing three absorbers in different planes.

layer of the cylindrical mesh. The positions of these cross-sectional planes with respect to the cylindrical object are indicated in Fig. 2. The target image, showing the placement of the absorbers in the image planes, is shown in Fig. 3. On a SPARC Ultra (165-MHz, 256-Mbytes RAM) the run time per iteration per source is 20 s, regardless of the number of measurements.

Figures 4–7 show the images obtained from one-, two-, three-, and five-layer intensity ( $E$ ) data after 150 iterations of the CG inverse solver. The positions of the measurement layers with respect to the central plane of the cylinder are listed in Table 1. The images are scaled to a common range 0.023 (black) to 0.038 (white).

When a conventional single-plane measurement arrangement is used in the central plane of the cylinder, the reconstruction algorithm recovers the object in the imaging plane (in the 12 o'clock position), with slight oscillatory artifacts and cross talk into the neighboring planes, but fails to localize any of the out-of-plane objects (Fig. 4). Note that a reconstruction from data collected in one single plane is funda-

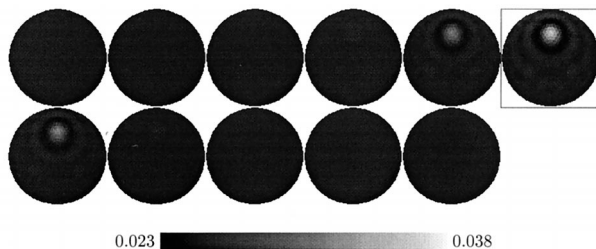


Fig. 4. 3D reconstruction from  $16 \times 16 \times 1$  (single-plane) intensity data.

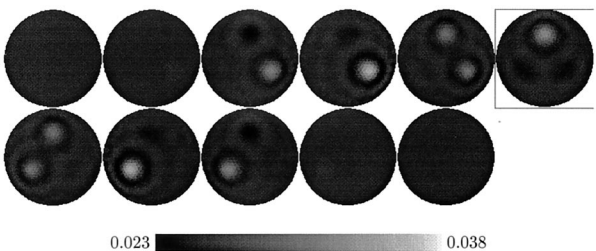


Fig. 5. 3D reconstruction from  $16 \times 16 \times 2$  (two-plane) intensity data.

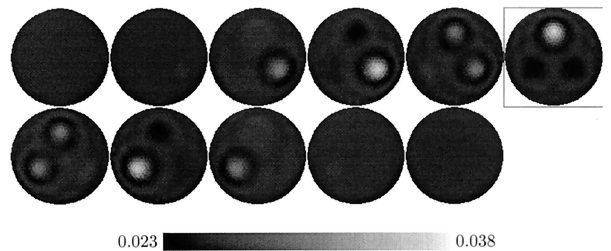


Fig. 6. 3D reconstruction from  $16 \times 16 \times 3$  (three-plane) intensity data.

mentally unable to give a  $z$  resolution, and if used to drive a 3D reconstruction scheme, it can only generate solutions that are symmetric in this plane.

In our example, all the multiplane reconstructions recover all the objects with similar success, although the peak values of the perturbations are recovered best from five-plane data (Figs. 5–7). To allow a quantitative comparison, we use the  $L_2$  norm of the difference between target image and reconstructed images:

$$\varepsilon = \left[ \int_{\Omega} |\mu_a^{\text{target}}(\mathbf{r}) - \mu_a^{\text{recon}}(\mathbf{r})|^2 d\mathbf{r} \right]^{1/2}, \quad (8)$$

which corresponds to the integral of the pointwise rms image error over the object. The choice of measure in the solution space is a topic that merits further attention but is beyond the scope of this paper. Here we use the  $L_2$  norm because it is implicitly the norm minimized in underdetermined generalized inverses.

Figure 8 shows  $\varepsilon$  as a function of the CG iteration. As expected, the single-plane reconstruction produces a poor solution norm because only one of the three objects is recovered. A large improvement is achieved by going to two planes, and more so by going to three planes. However, the three-plane and five-plane case give similar results, showing that image quality cannot be arbitrarily improved simply by adding more measurements.

To demonstrate the influence of the data type employed in the reconstruction, we repeated the single-plane reconstruction ( $16 \times 16 \times 1$  configuration), but using  $\langle t \rangle$  data. Figure 9 shows the reconstruction result after 150 CG iterations. A comparison with the corresponding  $E$  reconstruction in Fig. 4 shows

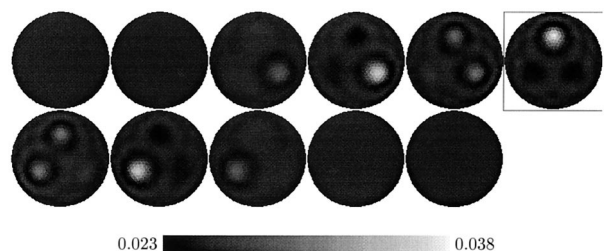


Fig. 7. 3D reconstruction from  $16 \times 16 \times 5$  (five-plane) intensity data.

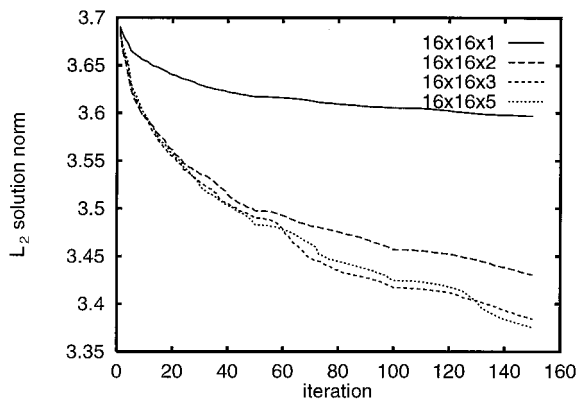


Fig. 8. Image norms for 3D reconstructions from one-, two-, three-, and five-layer intensity data as a function of CG iteration.

that the images look qualitatively similar, but the  $\langle t \rangle$  reconstruction obtains a higher object contrast. This is confirmed by a comparison of the image norms of these two cases in Fig. 10, which shows a significant improvement in the reconstruction performance on a per iteration basis for  $\langle t \rangle$  data. This must be offset, however, against the reconstruction run time because the forward model requires approximately twice as long for calculating mean time data than intensity data.

The noiseless conditions discussed so far represent an ideal case. The effect of noise in the data is demonstrated in Fig. 11, where we compare the data and solution norms for reconstructions from noiseless

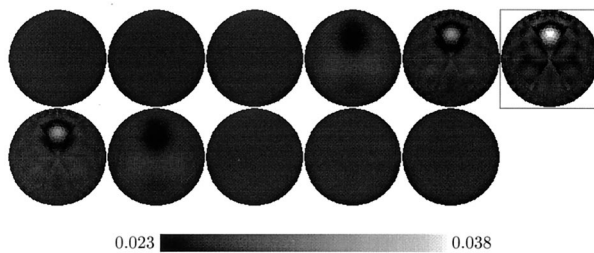


Fig. 9. 3D reconstruction from  $16 \times 16 \times 1$  (single-plane)  $\langle t \rangle$  data.

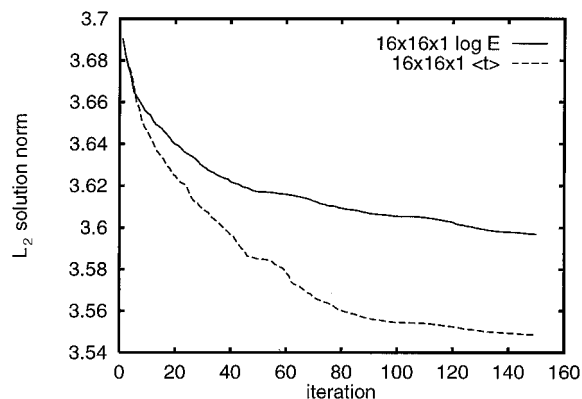


Fig. 10. Comparison of image norms for single-plane reconstructions from intensity ( $E$ ) and mean time-of-flight ( $\langle t \rangle$ ) data.

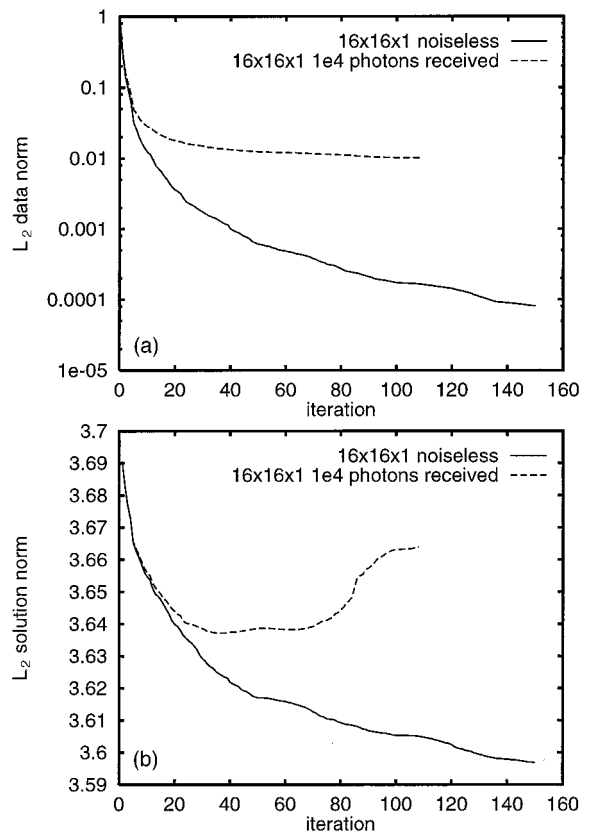


Fig. 11. Comparison of (a) data norm and (b) solution norm of  $16 \times 16 \times 1$  reconstruction from noiseless data and data with added noise, assuming  $10^4$  photons received at each measurement site.

data with reconstructions from data with added noise. We generated noise using a noise model presented previously,<sup>37</sup> under the assumption that  $10^4$  photons were collected at each measurement site. As expected, we found that, in the presence of noise, the data error cannot be reduced to the same level as in the noiseless case. A stopping criterion based on the gradient of the data norm would sensibly terminate the reconstruction between iteration 20 and 40. The solution error reaches a minimum at iteration 30.

### C. Two-Dimensional Reconstructions from Three-Dimensional Data

Of particular interest for practical applications of optical imaging is the question whether and to what extent it is possible to reconstruct data obtained from a real (3D) experiment with a 2D inverse model. If they can be applied, 2D models are faster by orders of magnitude compared with 3D models, which is a key factor in clinical applications.

We consider the following case: Let the data vector consist of measurements in the central plane of the cylindrical object, as generated with the 3D forward model. However, instead of using the (correct) 3D image algorithm to reconstruct the solution within the whole of the cylinder, we now employ a 2D

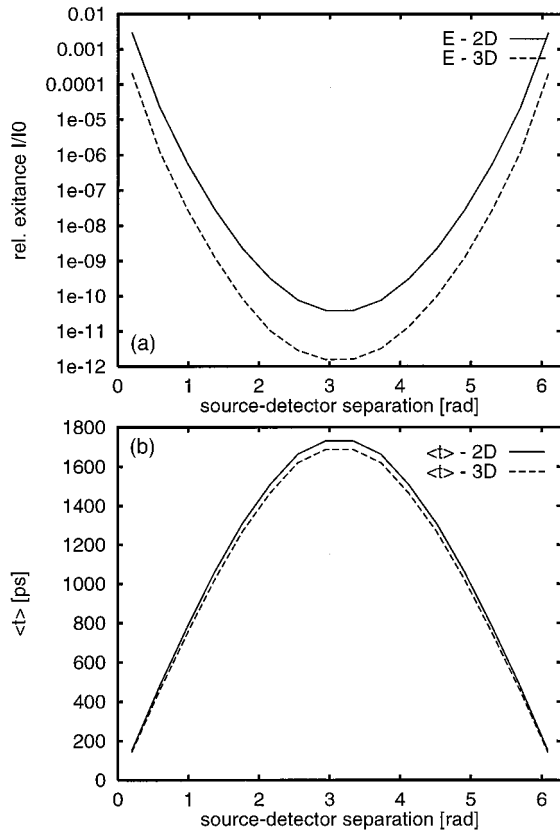


Fig. 12. Comparison of (a)  $E$  and (b)  $\langle t \rangle$  data for the homogeneous case, generated in the central plane of the cylinder with the 3D forward model and data generated from a circular object with the 2D forward model.

model to reconstruct the central plane only. In this case we expect artifacts in the image because the light propagation models used in the forward and inverse algorithms are mismatched. However, such artifacts may be acceptable up to a certain degree, considering the much higher speed of the 2D reconstruction.

To obtain an estimate of the extent of the mismatch of the 2D and 3D light transport models, we first compare 2D data obtained on a homogeneous circle with 3D data obtained in a plane of a homogeneous cylinder, using the same optical coefficients. Figure 12 shows the data types  $E$  and  $\langle t \rangle$  for a single source, as a function of the angular source-detector separation for both the 2D and the 3D cases, and Fig. 13 shows the ratio of 2D against 3D data for these measurement types. We find that for both  $E$  and  $\langle t \rangle$  the 2D/3D ratios are greater than 1 but show different profiles for the two data types and, more importantly, have a significantly different magnitude. The ratio is close to 1 for  $\langle t \rangle$  but has a value of approximately 20 for  $E$ . From these results we anticipate that a 2D reconstruction from 3D mean time data should produce better results than from 3D intensity data.

This assumption is confirmed by the reconstruction results. Figure 14 shows the 2D reconstruction of the central plane of the cylinder from different 3D

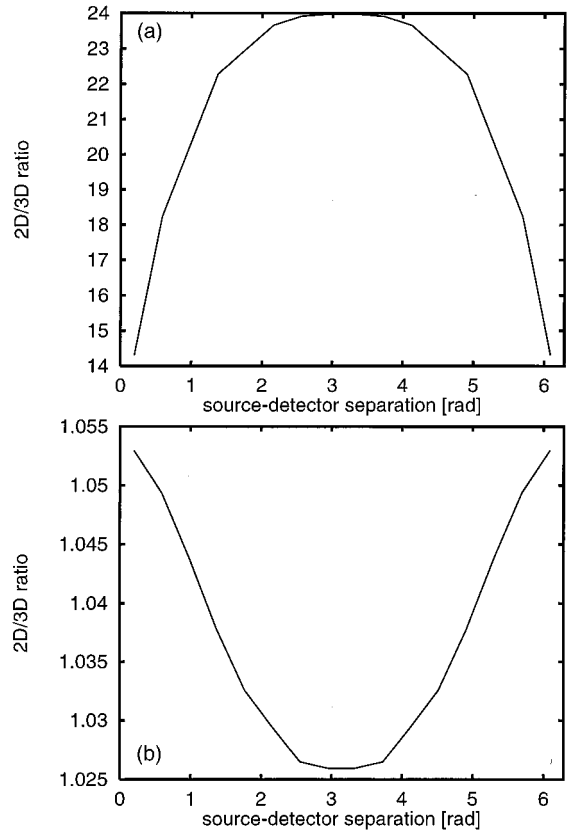


Fig. 13. Ratio of 2D/3D (a) intensity and (b) mean time data as a function of source-detector separation.

data. Reconstruction from  $E$  data [Fig. 14(a)] is dominated by boundary artifacts and completely fails to recover the object, whereas the reconstructions from  $\langle t \rangle$  [Fig. 14(b)], despite still showing some artifacts, clearly manages to localize the object.

It may be possible to improve the reconstruction results from mismatched data by preprocessing the 3D data. As an example, we fitted fourth-order polynomials to the ratio of 2D/3D intensity and the mean time data ratio in Fig. 13 and then used these polynomials to scale the 3D intensity and mean time data obtained in the central plane of the cylinder for the inhomogeneous case. We then used the 2D reconstruction scheme to reconstruct the plane from the modified data. The result is shown in Figs. 14(c) and 14(d) for  $E$  and  $\langle t \rangle$ , respectively. For  $E$ , the object is now found by the reconstruction, despite the appearance of severe ring artifacts. For  $\langle t \rangle$ , the artifacts are significantly reduced, and the object contrast is improved in comparison with the original reconstruction. The improvement is also apparent in the graphs in Fig. 15, which show cross sections along the vertical diameters of the images in Fig. 14 for  $E$  [Fig. 15(a)] and  $\langle t \rangle$  [Fig. 15(b)], both for reconstructions from original and fitted data. The  $L_2$  solution norms of the images obtained from the original and fitted data after 50 iterations are shown in Table 2. We found that, for the reconstruction from  $E$ , the norm increases compared with the homogeneous starting

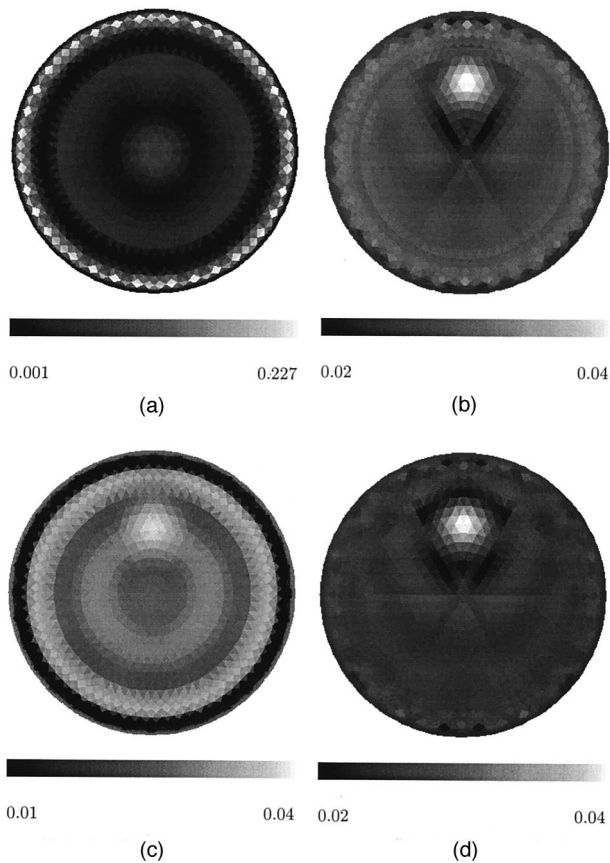


Fig. 14. Reconstruction of the central plane of the cylinder from single-plane data with the 2D reconstruction method. Data types: (a)  $E$  and (b)  $\langle t \rangle$ . The bottom row contains reconstructions from data modified with polynomial fit to 2D/3D homogeneous data to account for model mismatch: (c) fitted  $E$  and (d) fitted  $\langle t \rangle$ .

distribution, to different extents for original and fitted data. This indicates that the images are dominated by artifacts. In the case of reconstructions from  $\langle t \rangle$ , the norm is virtually unchanged when original data is used but is improved for fitted data. This suggests that the  $L_2$  norm is not the only factor to consider when assessing image quality.

Obviously, this fitting method is not universally applicable because the scaling function depends on the object size and geometry and on the optical parameters and would therefore have to be recomputed for each new problem, which is not feasible. However, it may be possible to obtain approximate scaling functions from phantom reference measurements, thus increasing the applicability of 2D reconstruction methods to experimentally obtained data.

#### D. Mismatched Reconstruction from Difference Data

A considerably simpler problem than the reconstruction of absolute values, as discussed so far, is the reconstruction of a difference image from difference data. In this case we have two sets of data, obtained either from the same object at two different times, between which the object may have undergone some change, or from two different objects of the same shape but different optical properties. Difference

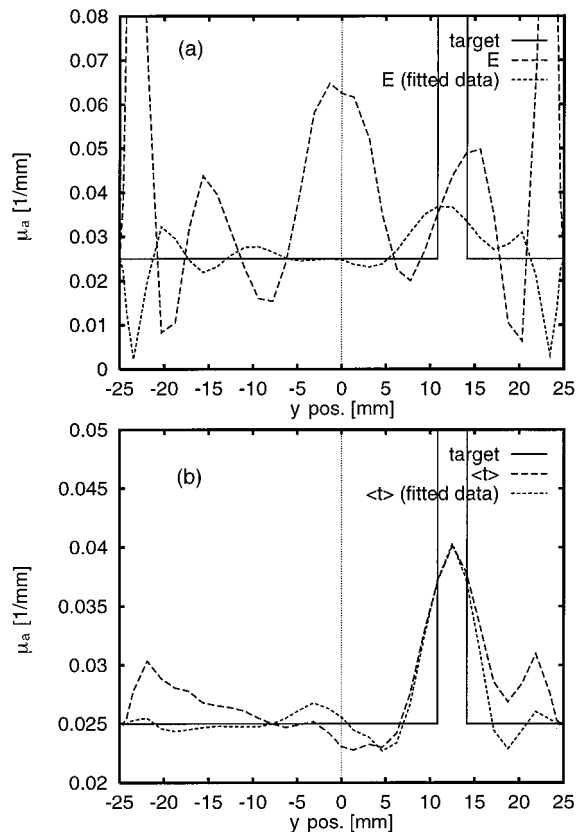


Fig. 15. Cross sections along the vertical diameter of images in Fig. 14: (a)  $E$  and (b)  $\langle t \rangle$ .

reconstructions eliminate many of the potential error sources present in absolute reconstructions, such as imperfectly known object outlines or source and detector placements. They should also reduce the effect of the model mismatch in 2D reconstructions from 3D data. Examples where this type of reconstruction problem may arise are continuous monitoring of the head when only changes in the optical parameters from a given baseline are of interest, or cases in which a calibration measurement on a phantom object with known optical properties and the same shape as the test object is available. In the special case in which for one of the measurements the corresponding parameters are known, absolute val-

Table 2. Solution Norms for 2D Reconstructions from 3D Data after 50 Iterations<sup>a</sup>

Data		$L_2$ Solution Norm
Original data	$E$	1.9367
	$\langle t \rangle$	0.2348
Fitted data	$E$	0.388597
	$\langle t \rangle$	0.2035
Difference data	$E$	0.233422
	$\langle t \rangle$	0.2027

<sup>a</sup>Norm for the homogeneous initial parameter distribution was 0.2349 in all cases.

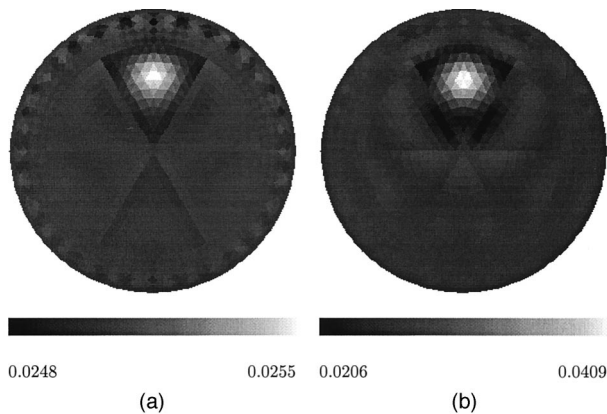


Fig. 16. As Fig. 14 but using homogeneous reference data and reconstructing for parameter differences only. These images were scaled individually because of their different dynamic ranges. Data types: (a)  $E$  and (b)  $\langle t \rangle$ .

ues for all other reconstructions can be obtained by simply adding the reconstructed differences to the reference parameter set.

We repeat the previous 2D reconstructions from 3D data, but this time we assume to possess reference data for the homogeneous case (no absorbing cylinders present). The data used in the reconstruction are the differences between the inhomogeneous and homogeneous data, and the reconstruction algorithm recovers the difference between the inhomogeneous and homogeneous parameter distributions. These are then added to the homogeneous background to obtain absolute values. Figure 16 shows the reconstruction results from  $E$  and  $\langle t \rangle$  difference data. In both cases the artifacts are significantly smaller than for the corresponding absolute reconstructions (see Fig. 14). Note, however, that the different data types vary significantly in their ability to recover absolute contrast value; the reconstruction from intensity shows little contrast of the perturbation. The images were therefore scaled individually. The cross sections along the vertical diameter are shown

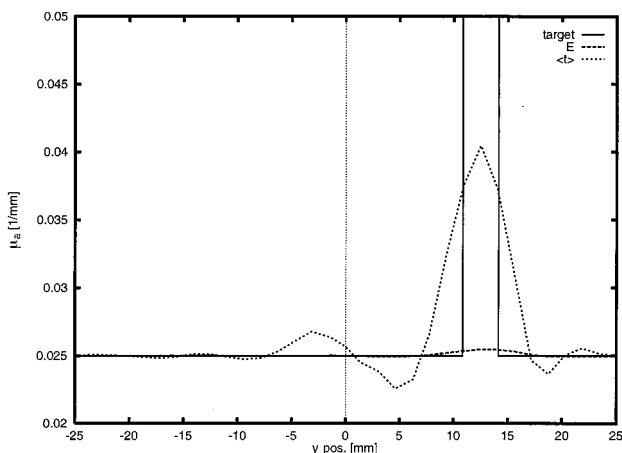


Fig. 17. Cross sections along the vertical diameter of images in Fig. 16.

in Fig. 17. The solution norms of the images are listed in the bottom section of Table 2. They show an improvement compared with the reconstructions from original and fitted data, although for the  $E$  case this is simply an effect of the small image contrast.

#### 4. Conclusion

In this paper we have presented a full 3D reconstruction scheme that can be applied to data obtained in experimental measurements. It employs a 3D light transport forward model that correctly describes the physics of the experimental setup used for the acquisition of the data it reconstructs its images from. Because the high degree of scattering in optical imaging does not allow one to confine photon propagation in a single plane as in x-ray-computed tomography, 3D models are necessary. The 3D model thus overcomes the problems of 2D models that necessarily ignore light propagation in the third spatial dimension. We have demonstrated the performance of the 3D reconstruction on the example of absorbing perturbations embedded in a cylindrical object. Reconstructions from data obtained by different measurement geometries show that a full 3D image can be recovered if multiplane measurement arrangements are used.

Because there is a strong interest in the use of 2D image reconstruction methods, because of their advantage in computation time and memory requirement over 3D methods, we have also investigated under which conditions a 2D reconstruction algorithm is able to reconstruct from 3D data. We found that, although the use of such a mismatched model necessarily leads to artifacts in the reconstructed image, the magnitude of these artifacts strongly depends on the measurement type used in the reconstruction process. Specifically, we have shown that a 2D reconstruction from 3D dc intensity data produces significantly worse results than one from 3D mean time-of-flight data. This can be attributed to the fact that intensity data depend to a higher degree on the problem dimension than mean time data.

We used the same reconstruction algorithm in each case. It may be that other algorithms or regularization may improve, for example, the 2D reconstruction from 3D data; however, it is our belief that real progress will come from further study of data types.

This research was supported by funding from Action Research and the Wellcome Trust.

#### References

1. A. D. Edwards, J. S. Wyatt, C. E. Richardson, D. T. Delpy, M. Cope, and E. O. R. Reynolds, "Cotside measurement of cerebral blood flow in ill newborn infants by near infrared spectroscopy," *Lancet* **2**, 770–771 (1988).
2. J. S. Wyatt, M. Cope, D. T. Delpy, C. E. Richardson, A. D. Edwards, S. C. Wray, and E. O. R. Reynolds, "Quantitation of cerebral blood volume in newborn infants by near infrared spectroscopy," *J. Appl. Physiol.* **68**, 1086–1091 (1990).
3. M. Tamura, "Multichannel near-infrared optical imaging of human brain activity," in *Advances in Optical Imaging and*

- Photon Migration*, R. R. Alfano and J. G. Fujimoto, eds., Vol. 2 of OSA Trends in Optics and Photonics Series (Optical Society of America, Washington, D.C., 1996), pp. 8–10.
4. R. A. de Blasi, M. Cope, C. E. Elwell, F. Safoue, and M. Ferrari, "Noninvasive measurement of human forearm oxygen consumption by near-infrared spectroscopy," *J. Appl. Physiol.* **67**, 20–25 (1993).
  5. J. C. Hebden and R. A. Kruger, "Transillumination imaging performance: a time of flight imaging system," *Med. Phys.* **17**, 351–356 (1990).
  6. A. H. Gandjbakhche, R. J. Nossal, and R. F. Bonner, "Theoretical study of resolution limits for time-resolved imaging of human breast," in *Advances in Laser and Light Spectroscopy to Diagnose Cancer and Other Diseases*, R. R. Alfano, ed., Proc. SPIE **2135**, 176–185 (1994).
  7. S. B. Colak, D. G. Papaioannou, G. W. 't Hooft, M. B. van der Mark, H. Schomberg, J. C. J. Paasschens, J. B. M. Melissen, and N. A. A. J. van Asten, "Tomographic image reconstruction from optical projections in light-diffusing media," *Appl. Opt.* **36**, 180–213 (1997).
  8. S. A. Walker, S. Fantini, and E. Gratton, "Back-projection reconstructions of cylindrical inhomogeneities from frequency domain optical measurements in turbid media," in *Advances in Optical Imaging and Photon Migration*, R. R. Alfano and J. G. Fujimoto, eds., Vol. 2 of OSA Trends in Optics and Photonics Series (Optical Society of America, Washington, D.C., 1996), pp. 137–141.
  9. S. A. Walker, D. A. Boas, and E. Gratton, "Photon density waves scattered from cylindrical inhomogeneities: theory and experiments," *Appl. Opt.* **37**, 1935–1944 (1998).
  10. M. A. O'Leary, D. A. Boas, B. Chance, and A. G. Yodh, "Experimental images of heterogeneous turbid media by frequency-domain diffusing-photon tomography," *Opt. Lett.* **20**, 426–428 (1995).
  11. C. L. Matson, N. Clark, L. McMackin, and J. S. Fender, "Three-dimensional tumor localization in thick tissue with the use of diffuse photon-density waves," *Appl. Opt.* **36**, 214–220 (1997).
  12. H. L. Graber, J. Chang, J. Lubowsky, R. Aronson, and R. L. Barbour, "Near infrared absorption imaging of dense scattering media by steady-state diffusion tomography," in *Photon Migration and Imaging in Random Media and Tissues*, B. Chance and R. R. Alfano, eds., Proc. SPIE **1888**, 372–386 (1993).
  13. S. R. Arridge, M. Schweiger, and D. T. Delpy, "Iterative reconstruction of near-infrared absorption images," in *Inverse Problems in Scattering and Imaging*, M. A. Fiddy, ed., Proc. SPIE **1767**, 372–383 (1992).
  14. H. Jiang, K. D. Paulsen, and U. L. Osterberg, "Optical image reconstruction using frequency-domain data: simulations and experiments," *J. Opt. Soc. Am. A* **13**, 253–266 (1999).
  15. B. W. Pogue, M. S. Patterson, H. Jiang, and K. D. Paulsen, "Initial assessment of a simple system for frequency domain diffuse optical tomography," *Phys. Med. Biol.* **40**, 1709–1729 (1995).
  16. M. Schweiger, S. R. Arridge, and D. T. Delpy, "Application of the finite-element method for the forward and inverse models in optical tomography," *J. Math. Imag. Vision* **3**, 263–283 (1993).
  17. K. D. Paulsen and H. Jiang, "Spatially-varying optical property reconstruction using a finite element diffusion equation approximation," *Med. Phys.* **22**, 691–701 (1995).
  18. H. Jiang, K. D. Paulsen, U. L. Österberg, and M. S. Patterson, "Frequency-domain near-infrared photo diffusion imaging: initial evaluation in multitarget tissuelike phantoms," *Med. Phys.* **25**, 183–193 (1998).
  19. U. Hampel and R. Freyer, "Fast image reconstruction for optical absorption tomography in media with radially symmetric boundaries," *Med. Phys.* **25**, 92–101 (1998).
  20. W. Cai, B. B. Das, F. Liu, F. A. Zeng, M. Lax, and R. R. Alfano, "Three dimensional image reconstruction in highly scattering turbid media," in *Optical Tomography and Spectroscopy of Tissue: Theory, Instrumentation, Model, and Human Studies II*, B. Chance and R. R. Alfano, eds., Proc. SPIE **2979**, 241–244 (1997).
  21. M. Keijzer, W. M. Star, and P. R. M. Storchi, "Optical diffusion in layered media," *Appl. Opt.* **27**, 1820–1824 (1988).
  22. S. R. Arridge and M. Schweiger, "The use of multiple data types in time-resolved optical absorption and scattering tomography (TOAST)," in *Mathematical Methods in Medical Imaging II*, J. N. Wilson and D. C. Wilson, eds., Proc. SPIE **2035**, 218–229 (1993).
  23. M. Schweiger and S. R. Arridge, "Optimal data types in optical tomography," in *Information Processing in Medical Imaging (IPMI'97 Proceedings)*, Vol. 1230 of Lecture Notes in Computer Science (Springer, New York, 1997), pp. 71–84.
  24. S. R. Arridge and M. Schweiger, "Direct calculation of the moments of the distribution of photon time of flight in tissue with a finite-element method," *Appl. Opt.* **34**, 2683–2687 (1995).
  25. M. Schweiger and S. R. Arridge, "Direct calculation with a finite-element method of the Laplace transform of the distribution of photon time of flight in tissue," *Appl. Opt.* **36**, 9042–9049 (1997).
  26. S. R. Arridge and W. R. B. Lionheart, "Non-uniqueness in diffusion-based optical tomography," *Opt. Lett.* **23**, 882–884 (1998).
  27. M. Schweiger, S. R. Arridge, M. Hiraoka, M. Firbank, and D. T. Delpy, "Comparison of a finite element forward model with experimental phantom results: application to image reconstruction," in *Photon Migration and Imaging in Random Media and Tissues*, B. Chance and R. R. Alfano, eds., Proc. SPIE **1888**, 179–190 (1993).
  28. S. R. Arridge, M. Schweiger, M. Hiraoka, and D. T. Delpy, "A finite element approach for modeling photon transport in tissue," *Med. Phys.* **20**, 299–309 (1993).
  29. M. Schweiger, S. R. Arridge, M. Hiraoka, and D. T. Delpy, "The finite element model for the propagation of light in scattering media: boundary and source conditions," *Med. Phys.* **22**, 1779–1792 (1995).
  30. C. Greenough and K. Robinson, *Finite Element Library* (Numerical Algorithms Group, Rutherford Appleton Laboratory, Chilton, Oxfordshire, UK, 1981).
  31. O. C. Zienkiewicz and R. L. Taylor, *The Finite Element Method*, 4th ed. (McGraw-Hill, London, 1987).
  32. M. Schweiger and S. R. Arridge, "The finite element method for the propagation of light in scattering media: frequency domain case," *Med. Phys.* **24**, 895–902 (1997).
  33. S. R. Arridge, "Photon measurement density functions. Part 1: Analytical forms," *Appl. Opt.* **34**, 7395–7409 (1995).
  34. S. R. Arridge and M. Schweiger, "Photon measurement density functions. Part 2: Finite element calculations," *Appl. Opt.* **34**, 8026–8037 (1995).
  35. S. R. Arridge and M. Schweiger, "A general framework for iterative reconstruction algorithms in optical tomography, using a finite element method," in *Computational Radiology and Imaging: Therapy and Diagnosis*, C. Borgers and F. Natterer, eds., Vol. 110 of IMA Volumes in Mathematics and Its Applications (Springer-Verlag, New York, 1998), in press.
  36. S. R. Arridge and M. Schweiger, "A gradient-based optimisation scheme for optical tomography," *Opt. Express* **2**, 213–226 (1998); <http://epubs.osa.org/oearchive/source/4014.htm>.
  37. S. R. Arridge, M. Hiraoka, and M. Schweiger, "Statistical basis for the determination of optical pathlength in tissue," *Phys. Med. Biol.* **40**, 1539–1558 (1995).